Chemistry Europe
European Chemical Societies Publishing
Batteries & Supercaps

RESEARCH ARTICLE OPEN ACCESS

Effect of Ca Doping on Structure and Electrochemical Properties of $Li_{3/8}Sr_{7/16}Hf_{1/4}Nb_{3/4}O_3$ Lithium-Ion Conductors

Alaa Alsawaf[1] | Mohana Veerraju Kante[1] | Philip Henkel[1] | Xiaomeng Pi[1] | Florian Stainer[2] | Martin Wilkening[2] | Leonardo Velasco[3] | Subramshu S. Bhattacharya[4] | Vladimir Sepelak[1,5] | Mamoru Senna[6] | Horst Hahn[1,7] | Torsten Brezesinski[1] | Miriam Botros[1]

[1]Institute of Nanotechnology, Karlsruhe Institute of Technology (KIT), Karlsruhe, Germany | [2]Institute for Chemistry and Technology of Materials, Graz University of Technology, Graz, Austria | [3]Universidad Nacional de Colombia sede de La Paz, Cesar, Colombia | [4]Nanofunctional Materials Technology Centre (NFMTC), Department of Metallurgical and Materials Engineering, Indian Institute of Technology Madras, Chennai, India | [5]Institute of Technology and Business in České Budějovice, České Budějovice, Czech Republic | [6]Department of Applied Chemistry, Keio University, Hiyoshi, Yokohama, Japan | [7]Materials Science and Engineering, University of Arizona, Tucson, Arizona, USA

Correspondence: Miriam Botros (miriam.botros@kit.edu)

Received: 24 November 2025 | **Revised:** 20 January 2026 | **Accepted:** 11 March 2026

Keywords: lithium conductivity | perovskite structure | solid electrolyte

ABSTRACT

Perovskite-structured solid electrolytes are promising candidates for next-generation solid-state lithium batteries due to their high ionic conductivity and structural stability. In this work, $Li_{3/8}Sr_{7/16-x}Ca_xHf_{1/4}Nb_{3/4}O_3$ solid electrolytes with various calcium contents ($x = 0$, 0.02, 0.05, 0.08, and 0.44) were synthesized via a sol–gel method, followed by high-temperature treatment. Comprehensive structural and electrochemical characterizations were conducted to elucidate the effect of Ca^{2+} substitution on material performance. Increasing Ca^{2+} concentration induced a structural transformation from cubic perovskite to an unidentified phase, suggesting a compositional limit for maintaining structural integrity. Among the investigated compositions, $Li_{3/8}Sr_{6.2/16}Ca_{0.05}Hf_{1/4}Nb_{3/4}O_3$ (LSCaHN) exhibited the highest ionic conductivity of 1.4×10^{-4} S cm^{-1} at room temperature, with negligible electronic contribution. Cyclic voltammetry revealed limited electrochemical stability against lithium metal, attributed to interfacial reactions that lead to electrolyte degradation. These findings highlight the importance of precise compositional design to balance structural stability and ionic transport in perovskite-type solid electrolytes for solid-state battery applications.

1 | Introduction

Solid-state batteries (SSBs) with inorganic solid electrolytes are expected to become one of the next-generation electrochemical energy storage devices. Compared to lithium-ion batteries that contain liquid electrolyte [1], SSBs promise safety advantages of a nonflammable and thermally stable solid compound with a potentially large electrochemical window, high density, and good mechanical strength [2]. Furthermore, various inorganic solid electrolytes, including garnet-type, perovskite-type, NASICON-type, LISICON-type, and sulfides, as well as antiperovskites are attractive due to their good Li-ion conductivity [1, 3–6]. Moreover, to realize the practical applications of SSBs, it is important to develop solid electrolytes that exhibit a low electronic contribution to the conductivity, low interfacial resistance between electrode and solid electrolyte, high ionic conductivity, and a wide electrochemical stability window [7]. Perovskite-type solid electrolytes (P-SEs) represent one of the candidates that can be applied in SSBs. However, P-SEs still suffer from several problems, such as high interfacial resistance, low total ionic conductivity, and poor stability against lithium metal [1].

Enhancing the low total ionic conductivity is of particular interest. In solid electrolytes, lithium ions move through vacancy hopping [8]. According to ion conduction principles, increasing the Li-ion concentration [9], as well as the size of the transport channels [9, 10], and ensuring the presence of vacancies can significantly enhance Li-ion conductivity. Different chemical compositions of P-SEs have been studied. The superionic $La_{2/3-x}Li_{3x}TiO_3$ (LLTO) has been reported with a high bulk conductivity of about 10^{-3} S cm^{-1} at room temperature [11–13]. However, LLTO is chemically unstable against lithium metal, because lithium insertion into LLTO at potentials around 1.8 V versus Li^+/Li results in the appearance of Ti^{4+}/Ti^{3+} redox, which limits battery performance [14]. The substitution of Ba^{2+}, Ca^{2+}, and Sr^{2+} on the A-site and Nb^{5+} and Zr^{4+} on the B-site could suppress the reduction of Ti^{4+} in the LLTO solid electrolyte [1]. Perovskite-type $Li_{3/8}Sr_{7/16}Hf_{1/4}Ta_{3/4}O_3$ (LSHT) reported by Huang et al. showed an ionic conductivity as high as 3.8×10^{-4} S cm^{-1} at room temperature. However, LSHT was evidently chemically unstable against lithium metal due to the reduction of Ta^{5+} to Ta^{4+} [15]. It has been shown that a simple substitution of zirconium by hafnium enhances the ionic conductivity from 2.7×10^{-4} S cm^{-1} for $Li_{3/8}Sr_{7/16}Zr_{1/4}Ta_{3/4}O_3$ [16] to 3.8×10^{-4} S cm^{-1} for LSHT. Bertrand et al. showed that incorporating calcium can increase the total ionic conductivity to $(3.6 \pm 1.0) \times 10^{-4}$ S cm^{-1} for the P-SE (LSHT) at room temperature [2]. Yu et al. synthesized perovskite-type $Li_{3/8}Sr_{7/16}Zr_{1/4}Nb_{3/4}O_3$ (LSZN) solid electrolyte with vacancies on the A-site, with a total ionic conductivity of 2.0×10^{-5} S cm^{-1} at 30°C [7]. Meanwhile, Kong et al.. showed that the ionic conductivity was enhanced by substituting zirconium with hafnium, reaching values of 2.91×10^{-5} S cm^{-1} at room temperature [1].

In this work, Li-Sr-Hf-Nb-O/(Ca-sub) (LSCaHN) solid electrolytes were prepared via sol–gel method. Ionic and electronic contributions to the conductivity were studied by AC impedance spectroscopy and DC polarization, respectively. The effect of composition on structure and conductivity of LSCaHN was investigated. Further, the materials were subjected to contact with lithium metal, to investigate their chemical stability. The electrochemical stability window was identified by means of cyclic voltammetry (CV). A comprehensive understanding of the stability of perovskite-type materials against lithium metal and related degradation mechanisms paves the way to designing new compositions with high total ionic conductivity, allowing application possibilities as separators, additives, or catholytes in SSBs. Calcium was selected as a dopant on the Sr site due to its identical valence state (Ca^{2+}/Sr^{2+}), which preserves charge neutrality and avoids the introduction of parasitic electronic conduction. Moreover, Ca is an earth-abundant, low-cost, and nontoxic element, offering clear advantages from both environmental and sustainability perspectives. Ca-containing oxide ceramics are also compatible with established ceramic processing and recycling pathways, enabling straightforward material recovery without complex separation steps. These characteristics make Ca substitution particularly attractive for the development of scalable and sustainable perovskite-based solid electrolytes.

2 | Experimental Section

A sol–gel reaction procedure was adopted to prepare the perovskite-type LSCaHN powders with five target compositions, namely $Li_{3/8}Sr_{7/16-x}Ca_xHf_{1/4}Nb_{3/4}O_3$ ($x = 0$, 0.02, 0.05, 0.08, and 0.44). The raw materials, including $LiNO_3$ (Sigma-Aldrich, 99%; 20 wt% excess), $SrNO_3$ (Thermo Scientific, 99%), $Ca(NO_3)_2 \times 4H_2O$ (Sigma-Aldrich, 99%), $HfCl_4$ (Sigma-Aldrich, 99.95%), $C_4H_4NNbO_9 \times xH_2O$ (Sigma-Aldrich, 99.99%), citric acid (CA) (Sigma-Aldrich, 99.5%), and ethylene glycol (EG) (Sigma-Aldrich, 99.0%), were selected as precursor materials. These materials were dissolved in 150 ml deionized water, with citric acid and ethylene glycol in a molar ratio of CA/EG = 1:4. The mixture was stirred at 150°C until a clear solution was obtained. At 150°C, an esterification reaction occurred between the hydroxyl groups of EG and the carboxylic acid groups of CA. Afterward, the temperature was increased to 300°C until a dark-brown gel was formed. The powder was calcined at 900°C for 12 h in an alumina crucible. Green cylindrical pellets of diameter of 8 mm and thickness ≈1.4 mm were consolidated by uniaxial pressing at 1.5 tons (≈293 MPa) for 1 min. Subsequently, the pellets were sintered at 1250°C for 12 h under air. The mother powder was used to cover the pellets to reduce possible lithium loss.

Powder X-ray diffraction (XRD) was used to determine the crystalline phase and lattice parameters of the samples (2022 Malvern Panalytical B.V.). A Cu-K_α radiation source was utilized in 2θ range from 10 to 90° with 0.02° step size at room temperature. Rietveld analysis was performed using the software FullProf Suite.

Scanning electron microscopy (SEM) (Zeiss Leo 1530) was used to analyze the morphology of the manually polished sintered pellets. The SEM was operated at an acceleration voltage of 10 kV, and a working distance 5 mm. Before SEM analysis, a thin gold layer (10 nm) was sputtered onto the samples (40 s, 30 mA) to avoid electrical charging.

Energy-dispersive X-ray spectroscopy (EDX) was used to investigate the chemical composition of the samples. The acceleration voltage was 20 kV, and the working distance was 8.5 mm.

Relative density values of ceramic samples were calculated geometrically and by the Archimedes immersion method using isopropanol as the immersion medium. The theoretical density was determined according to the crystallographic parameters obtained from Rietveld refinement to be 6.05 g cm^{-3}.

^{6}Li and ^{7}Li MAS NMR spectra were acquired on a Bruker Avance III 500 spectrometer equipped with an ultrashielded WB 500 MHz magnet (11.74 T), giving resonance frequencies of 73.6 MHz for ^{6}Li and 194 MHz for ^{7}Li. Spectra were referenced to the chemical shift of $CH_3COOLi \cdot xH_2O$. All measurements were performed at a spinning speed of 22 kHz and a bearing gas temperature of ≈298 K. ^{6}Li MAS NMR spectra were collected using a single $\pi/2$ pulse of 3.5 µs at 200 W. With a 4 s relaxation delay, 1200 scans were accumulated. For longer delays, the number of scans was reduced to avoid line broadening from magnetic-field drift; for a delay of 80s, 120 scans were used. For ^{7}Li spectra, a $\pi/2$ pulse of 1.6 µs at 200 W was applied. A relaxation delay of 40 s ensured full relaxation of all spectral contributions, and 40 scans were accumulated. The Ca^{2+}-doped $Li_{0.375}Sr_{0.437}Hf_{0.25}Nb_{0.75}O_3$ (LSHN) pellets were ground to a fine powder suitable for packing into 2.5 mm MAS rotors made of zirconia and fitted with Vespel caps.

X-ray photoelectron spectroscopy (XPS) measurements were performed using an Omicron XM 1000 MkII system equipped with an Al-Kα X-ray source (1486.6 eV). Photoelectrons emitted from the sample surface were collected using a SPECS Phoibos 150 analyzer. The X-ray source was operated at

15 kV and 20 mA. The acquired spectra were analyzed using CASA XPS software.

The ionic conductivity was measured from 25 to 50°C by alternating current electrochemical impedance spectroscopy (AC-EIS) in a (Solartron SI 1260) impedance/gain-phase analyzer in a frequency range from 1 MHz to 10 Hz and at an applied voltage amplitude of 50 mV under He atmosphere. The samples were 1–1.5 mm in thickness and between 7 and 8 mm in diameter. Both sides of the ceramic pellets were polished (grit size 1200) and sputter coated with Au (thickness around 80 nm) to act as ion blocking electrodes for conductivity measurements, and were mounted inside cryostat (Janis STVP-200-XG), as shown in Figure S1. Direct current polarization measurements were conducted with the same pellet configuration at 1 V for 48 h.

To examine the electrochemical stability window, a coin cell was assembled with LSCaHN serving as the cathode. The cell assembly process took place in an inert atmosphere within an Ar glovebox. For the cathode composition, LSCaHN, Super C65 carbon, and polyvinylidene fluoride (PVDF, Solvay, Solef 5130) were mixed in a weight ratio of 94:3:3. The mixture was dispersed in *N*-methyl pyrrolidone (NMP, Merck KGaA, ≥99.5%). A blender (Thinky, ARE250) was used to mix the slurry at 2000 rpm for 3 min until homogenized. The slurry was then applied onto 0.03 mm-thick Al foil using a film applicator (Erichsen Coatmaster, 510) with an operating rate of 1.5 mm s^{-1} and 140 µm slit size, and then dried at 120°C overnight in a vacuum drying oven (Binder, VDL53) to ensure adequate adhesion and removal of solvents. Electrodes were cut into 13 mm-diameter disks using an electrode cutter. In the cell configuration, Li metal was used as anode, glass fiber (Whatman, GF/D) as separator, and 95 µL of LP57 (1 M $LiPF_6$ solution in 3:7 by weight of ethylene carbonate and ethyl methyl carbonate) as electrolyte. CV measurements were carried out at a scan rate of 0.5 mV s^{-1} to investigate the cathode's voltage stability and electrochemical properties. This setup allowed for a detailed evaluation of LSCaHN under electrochemical cycling.

3 | Results and Discussion

3.1 | Compositional Consideration

The base material in LSZN or LSHN can be considered being $SrHfO_3$, which has a perovskite-type cubic structure. For LSHN, Hf^{4+} in $SrHfO_3$ can be substituted by Nb^{5+}, while Sr^{2+} can be partially substituted by Li^+. Hence, the substituted perovskite-type material can be written as $Li_zSr_{1-x}Hf_{1-y}Nb_yO_3$. Considering the charge-neutrality condition [7]

$$z + 2(1-x) + 5y + 4(1-y) = 6 \tag{1}$$

Thereby, $z = 2x - y$. The defect reaction equation can be written as

$$(2x-y)LiO_{0.5} + (1-x)SrO + (1-y)HfO_2 + yNbO_{2.5} \tag{2}$$

Using Kröger–Vink notation

$$(2x-y)Li'_{Sr} + (1-x)Sr^x_{Sr} + (1-y)Hf^x_{Hf} + y\,Nb_{Hf} + (y-x)V''_{Sr} + 3O^x_O$$

According to the ion diffusion relationship, the ionic conductivity can be expressed as

$$\sigma = n\,q\,\alpha \tag{3}$$

where n is the charge-carrier concentration, q the number of charges, and α the mobility of Li^+. In the mechanism of free vacancy migration for the diffusion of Li^+, σ is directly proportional to the product of Li^+ concentration (i.e., $c(Li'_{Sr}) = 2x - y$) and A-site vacancy concentration (i.e., $c(V''_{Sr}) = y - x$). Thus, Equation (3) can be written as

$$\sigma = K\,c(Li'_{Sr})c(V''_{Sr}) = K(2x-y)(y-x) \tag{4}$$

where K is a proportionality constant. Therefore, the conductivity is a function of a curved surface with regard to x and y, taking $y =$ constant. The first derivative of the conductivity is represented by

$$\frac{d\sigma}{dx} = K(3y - 4x) \tag{5}$$

Therefore, when this derivative is equal to zero $x = \frac{3}{4}y$.

3.2 | Crystal Structure and Microstructure

The XRD patterns collected from the $Li_{3/8}Sr_{7/16-x}Ca_xHf_{1/4}Nb_{3/4}O_3$ ($x = 0.0$, 0.02, 0.05, 0.08, and 0.44) samples are shown in Figure S2 (Supporting Information). For all LSCaHN samples, the main reflections belong to the cubic perovskite structure. In addition, a small HfO_2 impurity phase was found, with its fraction increasing with increasing Ca^{2+} content. This phenomenon can be explained by the tolerance factor of the perovskite structure. The tolerance factor is calculated using the following equation

$$t = \frac{R_A + R_O}{\sqrt{2}(R_B + R_O)} \tag{6}$$

where t is tolerance factor of ABO_3 compounds, and R_A, R_B, and R_O are the radii of Li^+, Sr^{2+}, and Ca^{2+} on the A-site and of Hf^{4+} and Nb^{5+} on the B-site and the anion site O^{2-}. The values are shown in Table 1. It is evident that the tolerance factor is much lower than 1, which indicates that it is difficult to achieve a stable perovskite structure. The excess of Hf^{4+} prefers to form impurity phases, such as HfO_2. Furthermore, it is obvious that the (100) reflection of the Ca^{2+}-containing materials in Figure S2 shifts to higher 2-theta angles with increasing calcium concentration due to the smaller radius of Ca^{2+} (1.34 Å at CN = 12) relative to that of Sr^{2+} (1.44 Å at CN = 12), where CN is the coordination number. Rietveld refinement of the lattice parameters, as shown in Figure 1, revealed no significant changes for the samples with $x =$ 0, 0.02, and 0.05; however, the refinement could not be performed for $x = 0.08$, as the structure starts to decompose with increasing calcium content and becomes unidentifiable upon full replacement of strontium by calcium. The crystallite sizes were determined to be in the range from 107 to 126 nm for all samples.

SEM images of the LSCaHN pellets are shown in Figure 2 and indicate good intergranular contact. The grain size was 3–7 µm for the $Li_{3/8}Sr_{7/16-x}Ca_xHf_{1/4}Nb_{3/4}O_3$ ($x = 0$, 0.02, 0.05) samples; however, for $x = 0.08$ imaging showed a melting phase during

TABLE 1 | Tolerance factor, density, conductivity, and activation energy for the LSCaNH samples.

Samples	Lattice parameter/Å	Tolerance factor	$\sigma_{(25°C)}$/S cm^{-1}	Density/g cm^{-3}	Activation energy/eV
LSHNO	3.988	0.8175	1.7859E^{-5}	6.05	0.41
LSCa$_{0.02}$HNO	3.989	0.8172	1.21671E^{-4}	5.99	0.37
LSCa$_{0.05}$HNO	3.990	0.8167	1.42453E^{-4}	5.85	0.34
LSCa$_{0.08}$HNO	—	0.8033	4.79494E^{-5}	5.92	0.37

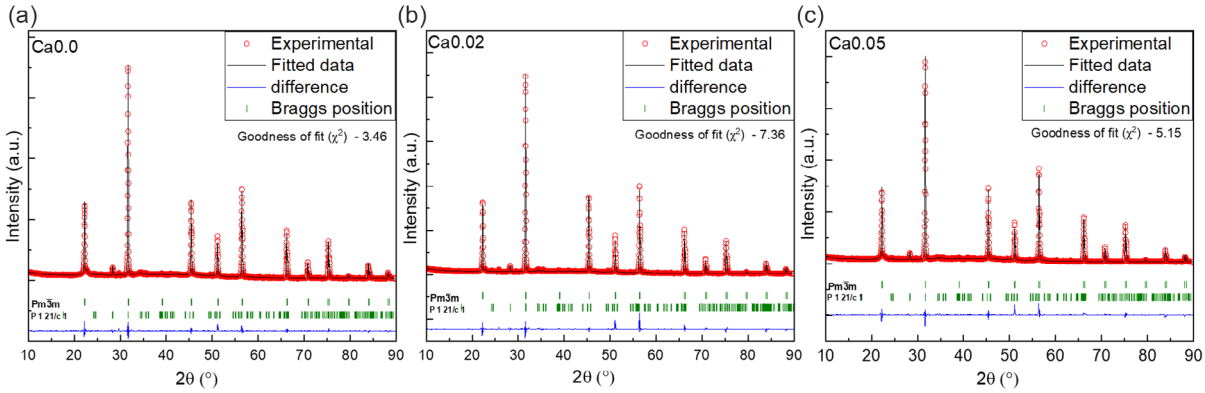

FIGURE 1 | XRD patterns and Rietveld refinement plots for the crushed pellets after sintering at 1250°C: (a) $x = 0$, (b) $x = 0.02$, and (c) $x = 0.05$. XRD = X-ray diffraction.

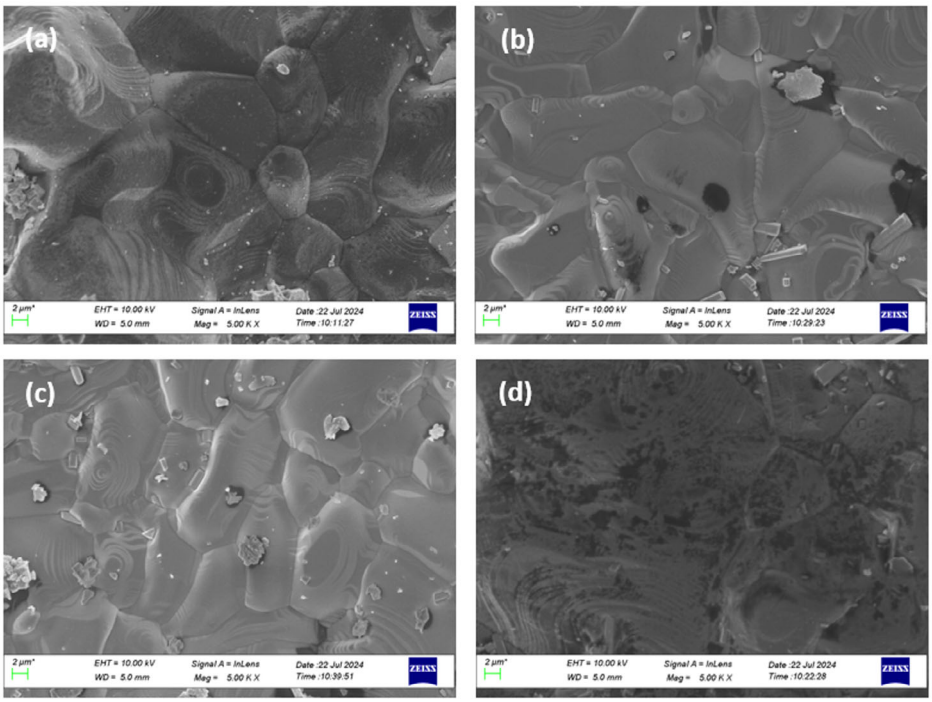

FIGURE 2 | SEM micrographs of the cross section of $Li_{3/8}Sr_{7/16-x}Ca_xHf_{1/4}Nb_{3/4}O_3$ samples sintered at 1250°C in air: (a) $x = 0$, (b) $x = 0.02$, (c) $x = 0.05$, and (d) $x = 0.08$. SEM = Scanning electron microscopy.

sintering and therefore the grain size could not be determined. This change in morphology has a significant influence on the electrochemical properties of the sintered samples.

The EDX elemental mapping of the sintered pellets, demonstrating a uniform distribution of Sr, Ca, and Nb throughout the material, is shown in Figure S3. The EDX map shows that segregation of Hf was observed, suggesting the presence of a secondary phase, likely HfO_2, as corroborated by the XRD measurements. For comparison, the EDX mapping of the sample without Ca, shown in Figure S4, does not show such segregation, indicating that Ca incorporation may play a role in the phase separation.

^{6}Li MAS NMR was performed on the undoped sample and on the sample with 0.05 Ca doping (Figure 3). Owing to the low natural abundance of the ^{6}Li isotope (7.5%), the average distance between

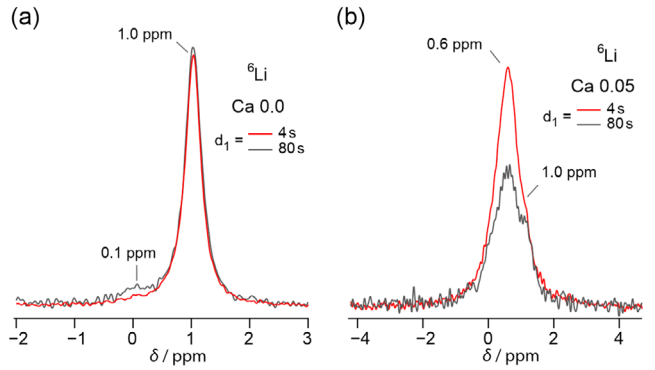

FIGURE 3 | ^{6}Li MAS NMR spectra of the perovskite samples without Ca (a) and with Ca doping (b), measured at a spinning speed of 22 kHz and at ambient temperature. For each sample, spectra were recorded using two relaxation delays, 4 and 80 s.

^{6}Li ions in the lattice is larger than for ^{7}Li, leading to weaker dipolar coupling. In addition, the quadrupole moment of ^{6}Li (spin $I = 1$) is by a factor of 50 smaller than that of ^{7}Li (spin $I = 3/2$). These characteristics often make ^{6}Li favorable for structural characterization. However, its lower abundance and lower intrinsic sensitivity require substantially longer measurement times.

Figure 3 shows the ^{6}Li MAS NMR spectra recorded with two different relaxation delays. In general, a longer delay allows a larger fraction of spins to relax before the subsequent 90° pulse, which is particularly relevant for slowly relaxing species. In the undoped perovskite (Figure 3a), a second signal at 0.1 ppm appears when using a delay of 80s, whereas it is absent with a 4 s delay. The main resonance (at ca. 1 ppm) remains unchanged, indicating that this component relaxes comparatively quickly. For the Ca-doped perovskite ($x = 0.05$, Figure 3b), two contributions at 1 and 0.6 ppm are resolved with a delay of 80s. Although the signal-to-noise ratio is lower for the measurement with $d_1 = 80$s, the longer delay improves the separation of the two components relative to the spectrum recorded with $d_1 = 4$ s.

Figure 4 compares the ^{6}Li MAS NMR spectra of the undoped and Ca-doped perovskite in one diagram. The main line of the undoped sample is narrower and symmetric, while the weaker secondary contribution appears below 1 ppm. In contrast, the Ca-doped sample exhibits at least two distinct components that merge into a broad, asymmetric line. The comparison suggests that the narrow resonance of the undoped material is also present in the Ca-doped sample but is broadened and overlapped by an additional contribution. We cannot exclude that even the narrow line reflects a small intrinsic distribution of local environments. Enhanced dynamics in the Ca-doped sample may also contribute to the observed line broadening.

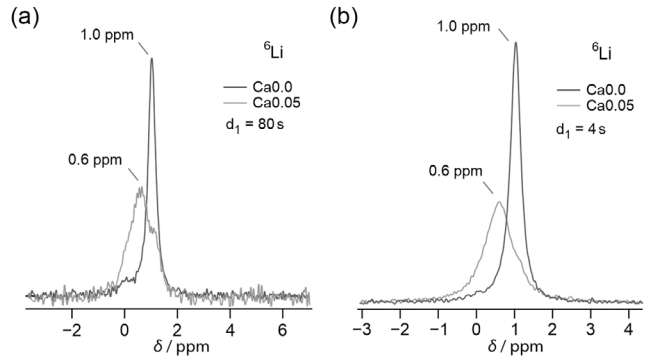

FIGURE 4 | ^{6}Li MAS NMR spectra measured at a spinning speed of 22 kHz and at ambient temperature. The Ca-doped perovskite is directly compared with the undoped sample. Spectra for both materials are shown for a relaxation delay of 80s (a) and 4 s (b).

Because of the higher natural abundance of ^{7}Li, stronger ^{7}Li–^{7}Li dipolar interactions lead to faster relaxation and higher signal intensity, but at the cost of reduced spectral resolution. Figure 5a compares the two samples directly, while Figure 5b,c shows the effect of different delay times for each sample. The undoped material exhibits a spectrum consisting of an intense, narrow resonance at 0.9 ppm, overlapped by a weaker signal at lower chemical shift. The intensity of the broad component increases when the delay time is extended from 1 to 20 s, indicating a slower relaxation process. However, no further change is observed between 20 and 200 s, demonstrating that all ^{7}Li sites are fully relaxed after 20 s. The Ca-doped sample shows a broader and slightly asymmetric resonance. Increasing the delay time only marginally affects the line shape, causing a slight increase in asymmetry at longer delays.

MAS NMR results indicate that Ca doping significantly alters the local Li environment and likely also the lithium occupancy. In addition, the doping increases the ionic conductivity, as shown in the following section and in Table 1. This behavior may arise from several factors.

1. Structural changes due to Ca incorporation:

Increasing the Ca content leads to structural modifications, as observed in the XRD patterns. Complete substitution of Sr by Ca results in an unidentified structure. Since Ca^{2+} (≈1.34 Å) is smaller than Sr^{2+} (≈1.44 Å), replacing Sr by Ca induces lattice shrinkage and further introduces distortions. These distortions may alter the size of diffusion channels or increase migration barriers, ultimately affecting ion transport.

2. Other conductivity mechanisms:

Although Li diffusion appears hindered, adding dopants may enhance the mobility of other charge carriers, which influence the overall conductivity but do not directly affect lithium migration. Additionally, changes in site occupancy and defect interactions caused by doping might further impact the ion migration pathways.

These factors suggest that while the conductivity increases, it is controlled by processes other than direct Li-ion mobility. More research, like computational modeling and advanced spectroscopy techniques, could shed light on how lattice changes, defect chemistry, and ion transport are correlated in the doped material.

3.3 | Electrical Properties

To further assess the impact of calcium incorporation on LSHN conductivity, AC impedance spectroscopy measurements were conducted on the LSHN and LSCaHN samples. The Nyquist plots of the electrochemical impedance for the samples are shown in Figure 6a. All samples exhibit a single semicircle in the high-frequency range, which makes it challenging to differentiate between bulk and grain boundary contributions to the conductivity. The spectra were fitted with type model (R(R//CPE)(R//CPE) CPE), as a result, the measured conductivity is considered as the

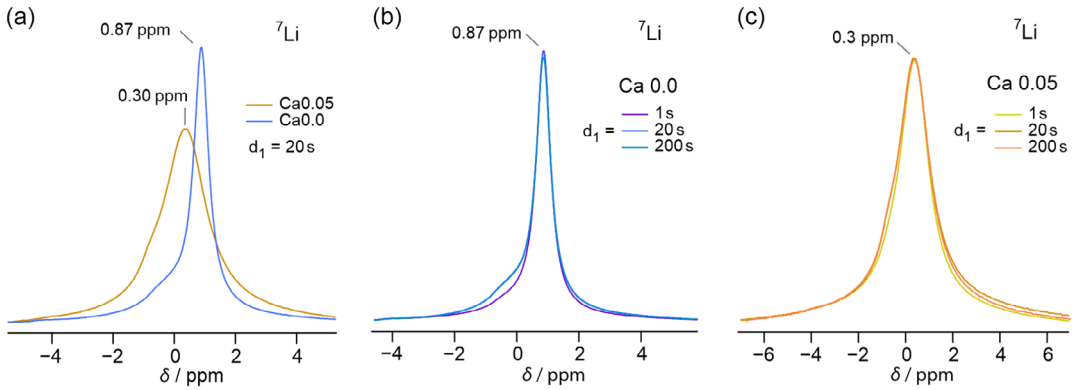

FIGURE 5 | ^{7}Li MAS spectra measured at a spinning speed of 22 kHz and at ambient temperature. The MAS NMR data show that Ca doping substantially modifies the local Li environment and likely affects the lithium site occupancy as well. (a) shows a direct comparison at a delay time of 20 s, (b) and (c) compare two different delay times of 20 and 200 s for each composition.

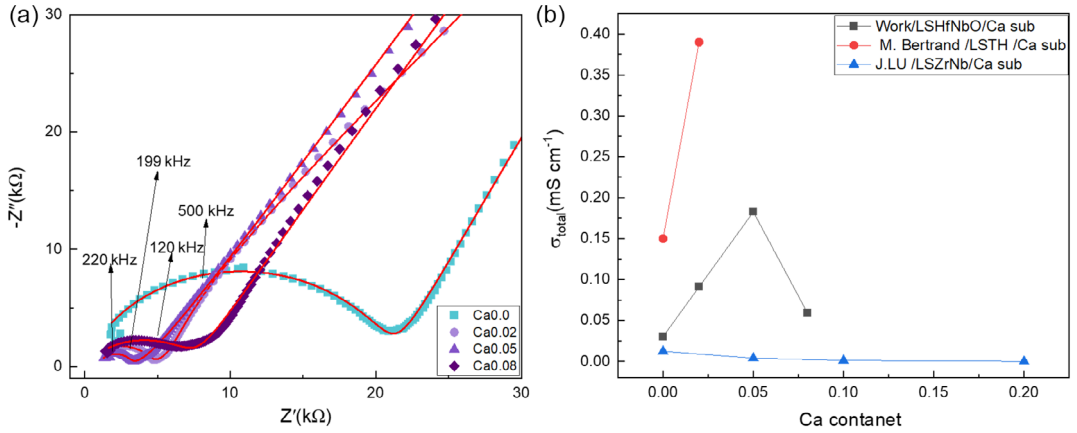

FIGURE 6 | (a) Nyquist plots for $Li_{3/8}Sr_{7/16-x}Ca_xHf_{1/4}Nb_{3/4}O_3$ at 25°C, where the frequencies at the semicircle maxima are indicated. (b) Comparison of total ionic conductivities for different systems, where the connecting lines are merely a guide to the eye [2, 10].

total conductivity of the material. The Nyquist plots have been normalized to account for the geometrical factors specific to each sample, with the data representing measurements taken at 25°C [2, 10]. The calculated total conductivity values are shown in Figure 6b and compared to other systems, in which calcium has been used as a dopant. This comparison provides insight into the influence of Ca doping on ionic conductivity of the different systems. The total conductivity was calculated as follows

$$\sigma = \frac{d}{R \times A} \tag{7}$$

where d is the thickness, A is the area of the pellet, and R represents the resistance. Figure 7a displays the temperature-dependent total conductivity of LSHN. It follows the Arrhenius equation, which is given as

$$\sigma = \frac{\sigma_0}{T} \times \exp\left(\frac{-E_a}{kT}\right) \tag{8}$$

where σ_0 is the pre-exponential factor (constant), k is the Boltzmann constant, and T is the absolute temperature in Kelvin. The plot of conductivity against $1000/T$ follows the expected linear trend. This indicates thermally activated ion conduction, where the slope corresponds to the activation energy (E_a) for ion transport in the LSHN samples, as shown in Figure 7b. The linearity of the plot suggests that no phase transitions occur in the measured temperature range, and the conduction mechanism remains consistent throughout this temperature regime.

One important prerequisite of advanced solid electrolytes is a negligible electronic partial conductivity (ideally $<10^{-8}$ S cm^{-1}) [17]. In this work, the electronic conductivity was determined by potentiostatic polarization. The applied voltage for polarization was 1 V, and Au electrodes were used as ion blocking electrodes. In Figure S5, the decrease in current with increasing polarization time can be seen. Finally, once the current reaches steady state, the electronic partial conductivity can be calculated using the following equation

$$\sigma_e = \frac{I \times d}{U \times A} \tag{9}$$

where, I is the steady-state current, U is the applied DC voltage (1 V), A is the area of the blocking electrode, and d represents the thickness of the pellet.

As expected, the electronic conductivities of the samples were in the order of 10^{-10} S cm^{-1}, which is about five orders of magnitude

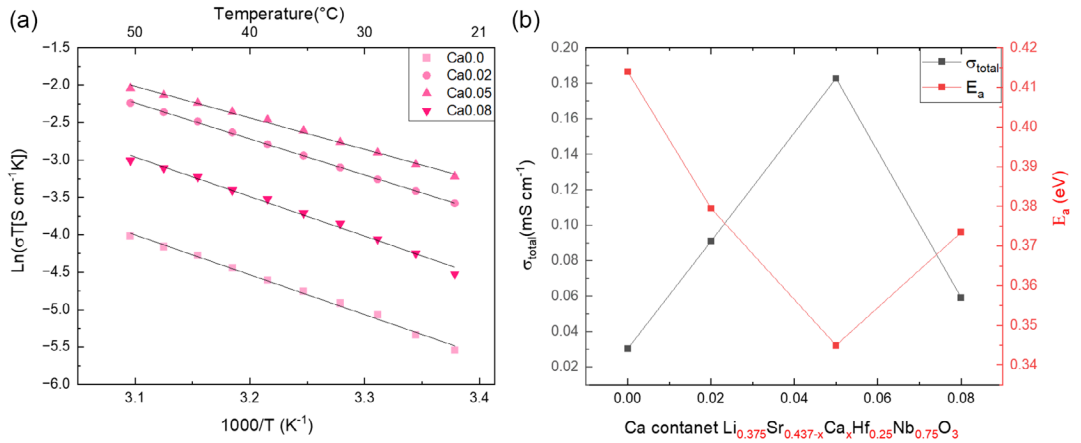

FIGURE 7 | (a) Arrhenius plots with black lines representing the linear fits and (b) total ionic conductivities at room temperature and activation energies for various doping levels, where the connecting lines are merely a guide to the eye.

lower than the measured total conductivity, showing that the electronic contribution to the conductivity can be neglected, which makes the materials suitable ionic conductors.

3.4 | Chemical Stability of LSCaHN Electrolyte against Lithium Metal

The color change of the LSCaHN pellet from white to black after a 15-minute exposure to lithium metal indicates that the material is chemically unstable in contact with lithium. This reaction with lithium metal suggests a decomposition process that compromises the integrity of the LSCaHN structure, rendering it unsuitable for applications where stable contact with lithium is required, such as in SSBs with a lithium metal anode.

To further investigate the nature and extent of this instability, XPS was employed to analyze the oxidation states of the constituent elements before and after lithium exposure. The XP spectra of the pellets for $x = 0$ and 0.05, shown in Figure 8, provide insight into the elemental composition and potential changes in oxidation states after contact with lithium. This analysis helps in understanding the decomposition products formed during the reaction and the specific interactions contributing to the material's instability in a lithium-rich environment. The Li 1s core-level peak is observed at a binding energy of ≈55 eV, as shown in Figure 8a. According to the literature, this binding energy is characteristic of both lithium carbonate and lithium oxide, indicating the possible presence of these lithium-containing species in the samples. Consistent with this observation, the C 1s and O 1s spectra shown in Figure 8b,c exhibit features corresponding to carbonate species, with peaks at ≈289 eV in the C 1s spectrum and ≈532 eV in the O 1s spectrum, respectively [18]. Furthermore, in the O 1s spectrum (Figure 8c), in addition to the carbonate-related peak, a distinct peak at ≈529 eV associated with metal oxide is also observed. This confirms the coexistence of lithium carbonate and metal oxide species on the sample surface, with relative fractions of ≈80% carbonate and 20% oxide as determined from the O 1s peak deconvolution. The existence of metal oxide is further observed in the XP spectra of Sr 3d, Nb 3d, and Hf 4f at 133, 206, and 16 eV, respectively [19, 20]. These peak positions closely match those of Sr 3d and Nb 3d in Sr_xNbO_3 and Hf 4f in HfO_2 [19, 20]. In Sr_xNbO_3, Sr has a stable +2 oxidation state, whereas Nb has a multivalent oxidation state between +4 and +5. Correlating the XP spectra with literature results, it can be deduced that Nb is present in multivalent form (between +4 and +5), Sr is +2, and Hf is +4 in the current material system. Interestingly, the peak positions of the XP spectra of Sr 3d, Nb 3d, Hf 4f, Li 1s, C 1s, and O 1s show no change with addition of Ca, indicating no changes in the valence state of these elements. This indifference in valence state is likely due to lack of difference in oxidation state between Sr^{2+} (host) with Ca^{2+} (dopant). Furthermore, XPS measurements were performed on $x = 0$ pellets after exposure to lithium metal and compared with the spectra of the as-synthesized pellets. The Li 1s spectrum shows a significantly higher intensity relative to the Sr and Nb 3d spectra, as shown in Figure S6a, indicating an increased lithium content in the system. Additionally, The O 1s spectrum of 0 Ca shown in Figure 8c indicates that the surface consists of ≈20% metal oxide and 80% carbonate species. In contrast, upon contact with lithium metal Figure S6b, the metal oxide contribution is significantly reduced to less than 2%, while the carbonate component dominates (>98%). This observation suggests that lithium deposited on the pellet surface is transformed into lithium carbonate upon contact. Despite the differences observed in the O 1s peak deconvolution, the Li 1s spectra in Figure S7c,d show no significant peak splitting or binding energy shift after contact with lithium. This is expected, as Li_2CO_3 and Li_2O possess nearly identical Li 1s binding energies, which can obscure any discernible peak splitting in the Li 1s spectra.

AC-EIS measurement of the $Li_{3/8}Sr_{7/16-x}Ca_xHf_{1/4}Nb_{3/4}O_3$ ($x = 0.05$) sample after contact with lithium metal shows evidence of changes in the grain boundary resistance. This observation suggests that the reaction between the material and lithium metal not only alters the surface chemistry, but also induces chemical and possibly morphological changes at the grain boundaries throughout the pellet thickness. Despite these changes, the activation energy for ion transport remains largely unaffected, as shown in Figure 9. This indicates that the bulk ionic pathways are relatively stable, and the changes are confined to grain boundary regions. The electronic conductivity of 2.2×10^{-10} S cm^{-1} was measured and is shown in Figure S8, showing no change in electronic behavior after lithium exposure.

SEM analysis, shown in Figure 10, was performed to further investigate the microstructural changes of the sample cross section before and after contact with lithium metal. The SEM images

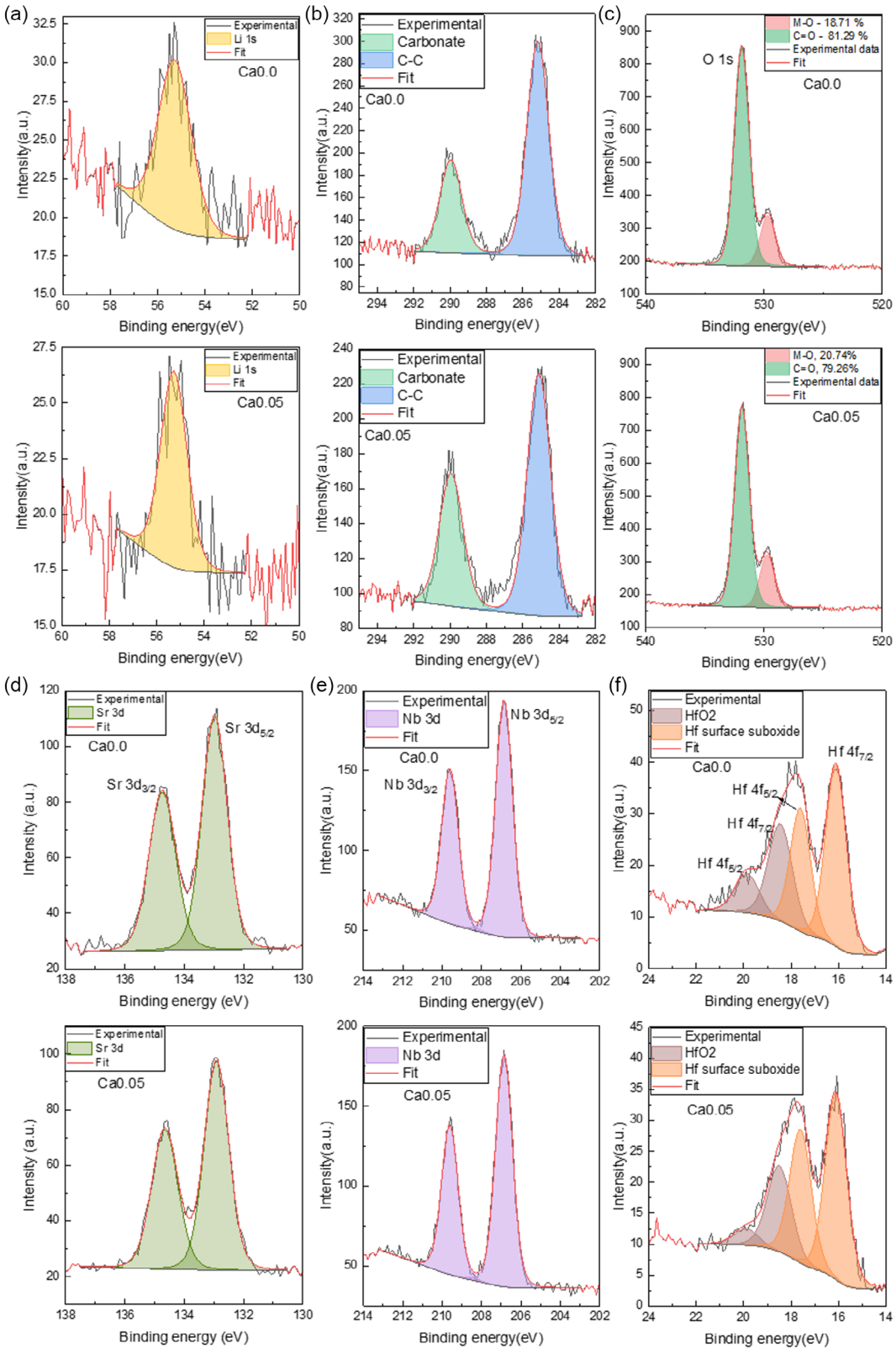

FIGURE 8 | X-ray photoemission spectra of pellets of $Li_{3/8}Sr_{7/16-x}Ca_xHf_{1/4}Nb_{3/4}O_3$ ($x = 0, 0.05$) before lithium metal contact, corresponding to elemental orbitals of (a) Li 1s, (b) C 1s, (c) O1s, (d) Sr 3d, (e) Nb 3d, and (f) Hf 4f.

revealed an increase in surface roughness of the grains after interaction with lithium, suggesting a change in morphology at the grain boundaries. The rough layer forming at the grain boundaries could be Li_2CO_3, as suggested by XPS, which can increase grain boundary resistance, as measured by EIS. Complementary EDX analysis confirmed the segregation of HfO_2 within the sample as detected before lithium exposure, images are shown in Figure S9.

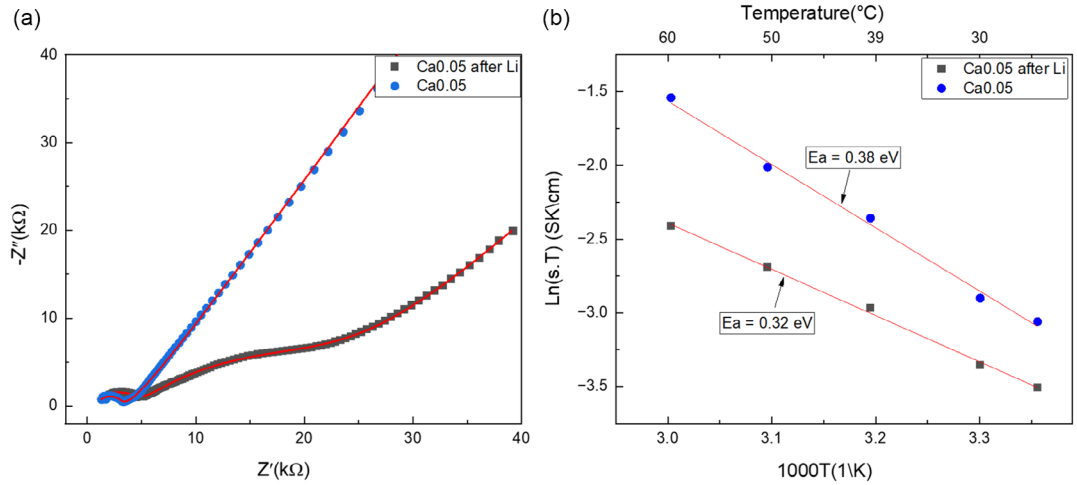

FIGURE 9 | (a) Nyquist and (b) Arrhenius plots for $Li_{3/8}Sr_{6.2/16}Ca_{0.05}Hf_{1/4}Nb_{3/4}O_3$ at 25°C before and after lithium exposure. Red lines represent the corresponding fits.

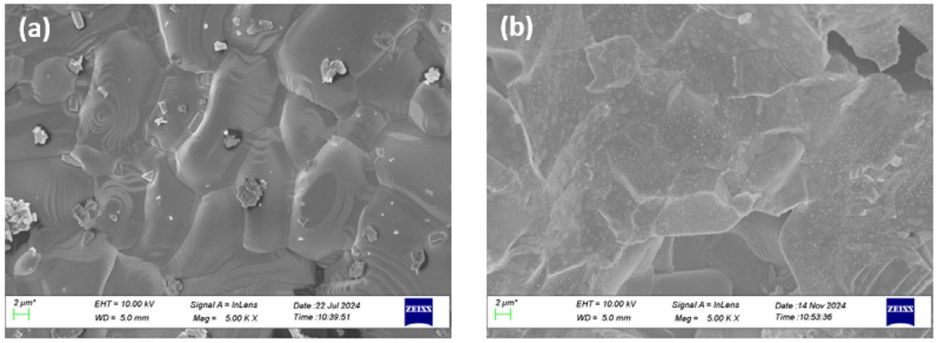

FIGURE 10 | SEM micrographs of the cross section of $Li_{3/8}Sr_{6.2/16}Ca_{0.05}Hf_{1/4}Nb_{3/4}O_3$ ceramics (a) before and (b) after lithium exposure. SEM = Scanning electron microscopy.

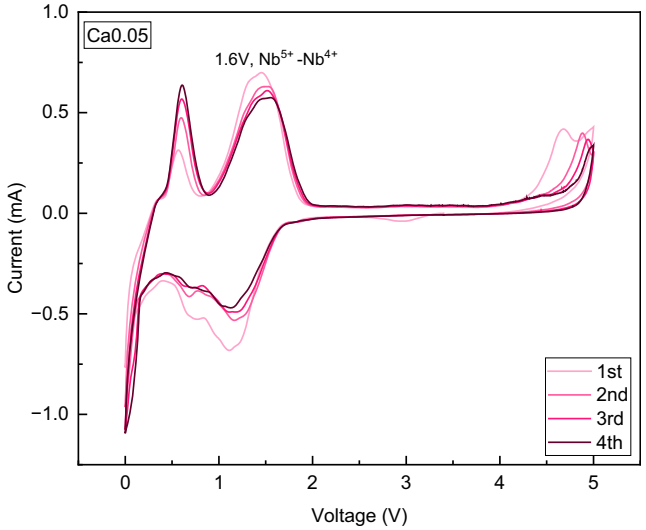

FIGURE 11 | Cyclic voltammograms of a Li|LP57|LSCaHN cell at a scan rate of 0.5 mV s^{-1}.

3.5 | Electrochemical Stability

CV of a half-cell is shown in Figure 11 using LSCaHN powder as the active material. The tests reveal that Li-ions can be inserted into this material in the potential range from 0.5 to 1.6 V versus Li^+/Li during the initial lithiation in a half-cycle, indicating that the LSCaHN electrolyte is, in addition to the chemical instability, electrochemically unstable when in contact with lithium metal at potentials below 1.6 V, thus limiting applications to higher potentials only. In addition, the CV curves display prominent oxidation and reduction peaks of Nb^{5+} in the potential range between 1.2 and 1.6 V [21], which confirms the presence of a reversible redox process. These peaks suggest that lithiation and delithiation of the material can occur repeatedly, maintaining the material's capacity for reversible electrochemical reactions within this potential range. LSCaHN solid electrolyte cannot be used in Li metal anode-based battery cells due to the narrow electrochemical stability window and chemical instability. However, a stable electrochemical window was identified between 2.0 and 4.0 V versus Li^+/Li, which can enable various applications in medium-voltage SSBs. As a separator between, e.g., titanate-based anode and $LiFePO_4$ (LFP) cathode, the perovskite-type electrolyte would facilitate efficient ion transport, thus minimizing interfacial resistance and enabling stable operation with suitable electrode-active materials. When employed as protective or buffer interlayer, their intrinsic ionic conductivity permits uninterrupted lithium migration while simultaneously suppressing parasitic interfacial reactions through electronic insulation and chemical robustness. As a cathode surface coating, it can preserve ion accessibility to the active material while providing a chemically stable barrier that mitigates electrolyte decomposition and

possible transition-metal dissolution. Further, in thin-film microbatteries, the perovskite electrolyte might support high rate capability and stable cycling.

4 | Conclusions

The perovskite-type oxide LSCaHN was successfully synthesized via the Pechini method and crystallizes in a cubic perovskite structure (space group $Pm\bar{3}m$). EDX analysis confirmed uniform distribution of Ca within the grains, as well as Hf segregation. The material exhibits a total Li-ion conductivity of 1.4×10^{-4} S cm^{-1} at 25°C, an activation energy of 0.38 eV and negligible electronic contribution to the conductivity, underscoring its potential as a solid electrolyte. Nevertheless, its electrochemical stability is limited to the range from 2.0 to 4.0 V versus Li^+/Li, and it demonstrates pronounced chemical reactivity toward lithium metal, which constrains its applicability in lithium-based systems.

^{6}Li and ^{7}Li MAS NMR reveal a redistribution of Li ions within the crystal lattice induced by doping. Broader NMR lines may also result from dynamic effects, which appear to be more pronounced in the Ca-doped sample. To further elucidate the influence of Ca on the total ionic conductivity and charge-carrier characteristics, particularly given the material's compositional complexity, complementary computational studies are warranted.

Overall, the combined structural, electrochemical, and compositional analyses highlight the intricate interplay between doping, stability, and transport properties in this perovskite-type electrolyte. These insights provide a foundation for rational compositional design and optimization of related materials for use in next-generation energy storage systems.

Author Contributions

Alaa Alsawaf: conceptualization (equal); data curation (lead); formal analysis (lead); investigation (lead); methodology (equal); visualization (lead); writing – original draft (lead). **Mohana Veerraju Kante:** data curation (supporting); formal analysis (supporting); writing – review & editing (supporting). **Philip Henkel:** investigation (supporting); methodology (supporting); writing – review & editing (supporting). **Xiaomeng Pi:** investigation (supporting); methodology (supporting). **Florian Stainer**: data curation (equal); formal analysis (equal); investigation (equal); methodology (equal); writing – original draft (equal). **Martin Wilkening:** formal analysis (supporting); methodology (equal); resources (supporting); validation (supporting); writing – review & editing (supporting). **Leonardo Velasco:** funding acquisition (equal); writing – review & editing (supporting). **Subramshu S. Bhattacharya:** funding acquisition (lead); resources (supporting); writing – review & editing (supporting). **Vladimir Sepelak:** funding acquisition (supporting); writing – review & editing (supporting). **Mamoru Senna:** validation (supporting); writing – review & editing (supporting). **Horst Hahn:** funding acquisition (lead); resources (lead); software (lead); supervision (lead); validation (equal); writing – review & editing (supporting). **Torsten Brezesinski:** resources (lead); validation (equal); writing – review & editing (equal). **Miriam Botros:** conceptualization (equal); formal analysis (equal); funding acquisition (equal); methodology (equal); project administration (lead); resources (supporting); supervision (lead); validation (lead); writing – review & editing (equal).

Acknowledgments

The authors would like to thank Deutsche Forschungsgemeinschaft (DFG), Project no. 424789449, grant no. HA 1344/45−1 and SE 1407/4-2, for the financial support. Subramshu S. Bhattacharya is grateful for the support provided by Indo-German DST-DFG collaborative project number DST/INT/DFG/P-01/2019. L.V.E. is grateful for the support provided by Universidad Nacional de Colombia (HERMES Project no. 57683 and 61001).

Open Access funding enabled and organized by Projekt DEAL.

Funding

This study was supported by Deutsche Forschungsgemeinschaft (Grant HA 1344/45-1 and SE 1407/4-2), Department of Science and Technology, Ministry of Science and Technology, India (Grant DST/INT/DFG/P-01/2019), Universidad Nacional de Colombia (Grant 57683 and 61001).

Conflicts of Interest

The authors declare no conflicts of interest.

Data Availability Statement

The data that support the findings of this study are available from the corresponding author upon reasonable request.

References

1. Y. Kong, Y. Li, J. Lu, and C. Hu, "Conductivity and Electrochemical Stability of Perovskite-Structured Lithium–Strontium–Niobium–Hafnium-Oxide Solid Li-Ion Conductors," *Journal of Materials Science: Materials in Electronics* 28 (2017): 8621–8629, https://doi.org/10.1007/s10854-017-6586-2.

2. M. Bertrand, L. Groleau, T. Bibienne, et al., "Calcium Substitution to Improve the Total Ionic Conductivity of the Li3/8Sr7/16Ta3/4Hf1/4O3 Perovskite-Type Electrolyte," *Solid State Ionics* 400 (2023): 116324, https://doi.org/10.1016/j.ssi.2023.116324.

3. R. Murugan, V. Thangadurai, and W. Fast Weppner," Lithium Ion Conduction in Garnet-Type Li7La3Zr2O12.," *Angewandte Chemie International Edition* 46 (2007): 7778–7781, https://doi.org/10.1002/anie.200701144.

4. Y. Zhao and L. L. Daemen, "Superionic Conductivity in Lithium-Rich Anti-Perovskites," *Journal of the American Chemical Society* 134 (2012): 15042–15047, https://doi.org/10.1021/ja305709z.

5. J. W. Fergus, "Ceramic and Polymeric Solid Electrolytes for Lithium-Ion Batteries," *Journal of Power Sources* 195 (2010): 4554–4569, https://doi.org/10.1016/j.jpowsour.2010.01.076.

6. Y. Wang and W.-H. Zhong, "Development of Electrolytes towards Achieving Safe and High-Performance Energy-Storage Devices: A Review," *ChemElectroChem* 2 (2015): 22–36, https://doi.org/10.1002/celc.201402277.

7. R. Yu, Q.-X. Du, B.-K. Zou, Z.-Y. Wen, and C.-H. Chen, "Synthesis and Characterization of Perovskite-Type (Li, Sr)(Zr, Nb)O3 Quaternary Solid Electrolyte for All-Solid-State Batteries," *Journal of Power Sources* 306 (2016): 623–629, https://doi.org/10.1016/j.jpowsour.2015.12.065.

8. C. Chen, "Stable Lithium-Ion Conducting Perovskite Lithium–Strontium–Tantalum–Zirconium–Oxide System," *Solid State Ionics* 167 (2004): 263–272, https://doi.org/10.1016/j.ssi.2004.01.008.

9. L. Truong, J. Colter, and V. Thangadurai, "Chemical Stability of Li-Stuffed Garnet-Type Li5 + *x*Ba*x*La3 − x*x*Ta2O12 (x = 0, 0.5, 1) in Water: A Comparative Analysis with the Nb Analogue," *Solid State Ionics* 247-248 (2013): 1–7, https://doi.org/10.1016/j.ssi.2013.05.013.

10. J. Lu, Y. Li, and Y. Ding, "Structure and Conductivity of Li3/8Sr7/16−xAxZr1/4Nb3/4O3 (A = Ca, Ba) Li-Ion Solid Electrolytes.," *JOM* 72 (2020): 3256–3261, https://doi.org/10.1007/s11837-020-04239-9.

11. Y. Inaguma, L. Chen, M. Itoh, and T. Nakamura, "Candidate Compounds with Perovskite Structure for High Lithium Ionic Conductivity," *Solid State Ionics* 70-71 (1994): 196–202, https://doi.org/10.1016/0167-2738(94)90309-3.

12. M. Itoh, Y. Inaguma, W.-H. Jung, L. High Chen, T. Nakamura, "High Lithium Ion Conductivity in the Perovskite-Type Compounds Ln12Li12TiO3, (Ln = La, Pr, Nd, Sm)," *Solid State Ionics* 70-71, Part 1 (1994): 203–207, https://doi.org/10.1016/0167-2738(94)90310-7.

13. Z. Yang, S. Suzuki, N. Tanibata, et al., "Efficient Experimental Search for Discovering a Fast Li-Ion Conductor from a Perovskite-Type $Li_x La_{(1-x)/3} NbO_3$ (LLNO) Solid-State Electrolyte Using Bayesian Optimization," *The Journal of Physical Chemistry C* 125 (2021): 152–160, https://doi.org/10.1021/acs.jpcc.0c08887.

14. S. Yan, C.-H. Yim, V. Pankov, et al., "Perovskite Solid-State Electrolytes for Lithium Metal Batteries," *Batteries* 7 (2021): 75, https://doi.org/10.3390/batteries7040075.

15. B. Huang, B. Xu, Y. Li, et al., "Li-Ion Conduction and Stability of Perovskite $Li_{3/8}Sr_{7/16}Hf_{1/4}Ta_{3/4}O_3$," *Acs Applied Materials & Interfaces* 8 (2016): 14552–14557, https://doi.org/10.1021/acsami.6b03070.

16. R. Inada, K. Kimura, K. Kusakabe, T. Tojo, and Y. Sakurai, "Synthesis and Lithium-Ion Conductivity for Perovskite-Type Li3/8Sr7/16Ta3/4Zr1/4O3 Solid Electrolyte by Powder-Bed Sintering," *Solid State Ionics* 261 (2014): 95–99, https://doi.org/10.1016/j.ssi.2014.04.005.

17. E. Zhao, F. Ma, Y. Jin, and K. Kanamura, "Pechini Synthesis of High Ionic Conductivity Li1.3Al0.3Ti1.7 (PO4)3 Solid Electrolytes: The Effect of Dispersant," *Journal of Alloys and Compounds* 680 (2016): 646–653, https://doi.org/10.1016/j.jallcom.2016.04.173.

18. K. N. Wood and G. Teeter, "XPS on Li-Battery-Related Compounds: Analysis of Inorganic SEI Phases and a Methodology for Charge Correction," *Acs Applied Energy Materials* 1 (2018): 4493–4504, https://doi.org/10.1021/acsaem.8b00406.

19. C. Morant, L. Galán, and J. M. Sanz, "An XPS Study of the Initial Stages of Oxidation of Hafnium," *Surface & Interface Analysis* 16 (1990): 304–308, https://doi.org/10.1002/sia.740160163.

20. K. Isawa, R. Itti, J. Sugiyama, N. Koshizuka, and H. Yamauchi, "Photoelectron Spectroscopic Study of Sr x NbO3," *Physical Review B* 49 (1994): 3534–3538, https://doi.org/10.1103/PhysRevB.49.3534.

21. B. M. Jager, L. Kortekaas, J. E. Ten Elshof, J.-W. G. Bos, M. Tromp, and M. Huijben, "Mixed-Phase Enabled High-Rate Copper Niobate Anodes for Lithium-Ion Batteries," *Journal of Materials Chemistry A* 13 (2025): 5130–5142, https://doi.org/10.1039/D4TA07548J.

Supporting Information

Additional supporting information can be found online in the Supporting Information section.